nuclear fusion
IAEA

PAPER • OPEN ACCESS

Characterizing core and edge turbulence regimes with fluctuation imaging diagnostics in Wendelstein 7-X

To cite this article: A. von Stechow *et al* 2026 *Nucl. Fusion* **66** 046014

OPEN ACCESS
IOP Publishing | International Atomic Energy Agency
Nuclear Fusion
Nucl. Fusion **66** (2026) 046014 (12pp)
https://doi.org/10.1088/1741-4326/ae4919

Characterizing core and edge turbulence regimes with fluctuation imaging diagnostics in Wendelstein 7-X

A. von Stechow[1,*], S.G. Baek[2], J.-P. Bähner[2], S. Ballinger[2], D. Cipciar[1], E.M. Edlund[3], G. Fuchert[1], O. Grulke[1,4], T. Gonda[5], S.K. Hansen[2], C. Killer[1], S. Kwak[1], M. Krychowiak[1], A. Langenberg[1], N. Pablant[6], E. Pasch[1], A. Pavone[1], M. Porkolab[2], J. Svensson[1], J.L. Terry[2], D. Zhang[1] and the W7-X Team[1,a]

[1] Max Planck Institute for Plasma Physics, 17491 Greifswald, Germany
[2] Plasma Science and Fusion Center, Massachusetts Institute of Technology, Cambridge, MA 02139, United States of America
[3] State University New York Cortland, Cortland, NY 13045, United States of America
[4] Technical University of Denmark, 2800 Kongens Lyngby, Denmark
[5] Auburn University, Auburn, AL 36849, United States of America
[6] Princeton Plasma Physics Laboratory, Princeton, NJ 08543, United States of America

E-mail: astechow@ipp.mpg.de

Received 12 December 2025, revised 30 January 2026
Accepted for publication 23 February 2026
Published 17 March 2026

Abstract

Two density fluctuation imaging systems, phase contrast imaging (PCI) and gas puff imaging (GPI) measure spatially resolved density fluctuations with high time resolution throughout the core plasma (PCI) and in the scrape-off layer (GPI) of the Wendelstein 7-X (W7-X) stellarator. Both systems combined give a comprehensive overview of overall fluctuation levels, spectral properties such as their distribution in frequency and wavenumber space as well as their spatial distribution. These tools are used to assess changes in density turbulence in three representative discharges that transition into stable divertor detachment by different strategies (impurity seeding, density ramping and power starvation). Several general trends are identified when the radiated power fraction is systematically increased: In the plasma edge, the line emission observed by GPI shifts radially inward with a drop in electron temperature, and normalized intensity fluctuation profiles follow this inward shift. Skewness and kurtosis of these edge fluctuations are reduced, indicating a reduction of large intermittent transport events, and poloidal phase velocities decrease in magnitude. These observations are consistent with a reduced power input into the plasma edge and a general reduction of turbulent activity. Core density fluctuation levels remain nearly constant in the impurity seeding scenario, indicating that detachment does not significantly impact turbulence there. However, a strong reduction in

[a] See Grulke *et al* 2024 (https://doi.org/10.1088/1741-4326/ad2f4d) for the W7-X Team.
[*] Author to whom any correspondence should be addressed.

the dominant outboard fluctuation phase velocity is observed that deviates from the previous interpretation of neoclassical radial electric field changes, showing that the core plasma is not completely unaffected. In the density ramp and power starvation scenarios, undesirable and irregular large-scale events arise clearly in both diagnostic systems as the radiative fraction is increased. Impurity seeding therefore seems to be a promising strategy on W7-X to achieve detachment without significantly altering core turbulence, especially when targeting a specific operating point in core density and heating power.

Keywords: Wendelstein 7-X, magnetic confinement fusion, turbulence, detachment, phase contrast imaging, gas puff imaging

(Some figures may appear in colour only in the online journal)

1. Introduction

Recent and ongoing experiments in the Wendelstein 7-X (W7-X) optimized stellarator indicate that turbulence plays a dominant role in energy and particle transport [1]. Specifically, successful neoclassical optimization has been demonstrated experimentally [2], and anomalous transport has been shown to be a dominant and performance-limiting transport channel in standard heating scenarios [3, 4]. Gyrokinetic simulation efforts of varying fidelity and complexity are investigating the underlying turbulence instabilites, their plasma parameter and magnetic geometry dependencies, and saturation mechanisms [5–9]. These are gradually establishing a basis for the theoretical understanding of the relevant anomalous heat and particle transport mechanisms. Fully consistent and quantitatively predictive modeling remains prohibitively expensive, and reduced models require careful validation against experimental observations. Experimentally understanding and mitigating the mechanisms driving turbulence is one of the primary goals of the W7-X research program, which aims to optimize the stellarator magnetic confinement concept leading to an economically attractive future steady-state reactor. A major goal of ongoing experimental program is the systematic study of turbulent microinstabilities in the available operational parameter space, both in terms of magnetic configuration and profile dependencies [10]. Turbulent transport can be characterized indirectly from equilibrium profiles by global power balance and transport studies, revealing large and often dominant anomalous heat and particle transport channels [4, 11]. More directly, turbulent fluctuations are measured by several diagnostic systems that have been implemented on W7-X with the goal of identifying and characterizing transport-relevant microinstabilities such as ion temperature gradient (ITG), trapped electron (TEM) and kinetic ballooning modes (KBMs) in the plasma core, as well as observe the role of filamentary structures in the scrape-off layer (SOL). In particular, two density fluctuation imaging systems, phase contrast imaging (PCI) and gas puff imaging (GPI) measure spatially resolved (and therefore wavenumber-resolved) density fluctuations with high time resolution throughout the core plasma (PCI) and in the SOL (GPI), respectively.

The paper focuses on results from the most recent experimental campaign OP2.1 (2022–2023), the first in which GPI was available. An attractive scenario to showcase the complementary features of both systems is that of stable divertor detachment, in which a steady-state plasma is modified by external actuators to increase the radiation at the plasma edge and reduce the heat load on the divertor target plates. For an attractive reactor-relevant scenario, detachment should ideally be a well-controlled plasma edge process compatible with sustained good performance in the core [12], especially regarding possible worsening of turbulence. Core and edge turbulence are characterized throughout the transition into detachment, providing a first indication that core density fluctuations remain largely unaffected when detachment is approached with care, while the radial localization of edge fluctuations shifts substantially with the moving radiation front.

In the following, the paper first introduces three representative W7-X discharges from a global perspective which transition into detachment via different routes in section 2, then describes the density turbulence imaging diagnostics used for detailed analysis in section 3, and presents observations from these in the three detachment scenarios in section 4 before summarizing their commonalities and differences in section 5.

2. Representative detachment discharges

In the OP2.1 campaign of W7-X, stable and controlled divertor detachment was achieved by three strategies: power starvation by reduction of heating power at constant density (stabilized by feedback-controlled gas puffing), a feedback-controlled density ramp by hydrogen puffing (the main gas used in W7-X) at constant heating power, or injection of strongly radiative impurities such as nitrogen, neon or argon into otherwise constant discharge parameters. In all three scenarios, the radiative fraction $f_{rad} = P_{rad}/P_{ECH}$, defined as the ratio of total radiated to heating power (in the presented cases only by electron cyclotron resonance heating, ECRH) increases nonlinearly with the external actuator. The transition into detachment is gradual, and characterized by a complex and fully three-dimensional interplay of edge ionization, plasma surface

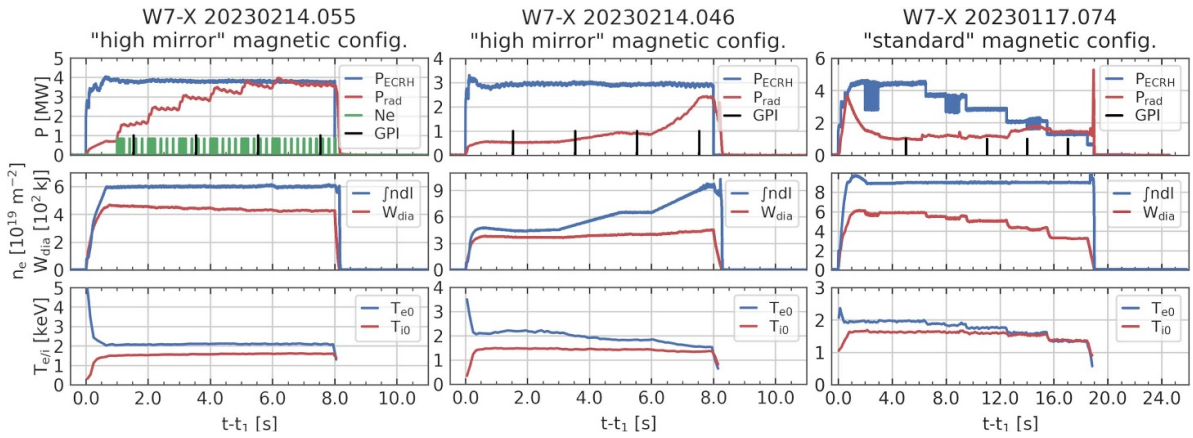

Figure 1. Summary time traces of plasma parameters during three discharges going into detachment. *Left:* Neon impurity seeding into a steady-state plasma at constant heating power and density into complete detachment around 6 s. *Center:* Feedback-controlled density ramp (hydrogen puffing) reaching detachment ($f_{rad} \approx 0.8$). *Right:* Power step-down at constant density into complete detachment at 16 s.

interaction processes and impurity radiation with a high value of $f_{rad} \sim 1$, as described in [12–14]. In summary, an externally forced change in the SOL power balance may reduce its temperature, and the intrinsic impurity line radiation zone (mainly from carbon) shifts radially inward, lifting off from the target into the SOL. As f_{rad} approaches 1, the radiation (and eventually ionization) front moves towards the closed flux surface region and may affect the core plasma. Further increasing radiation forces the discharge into either an operationally undesirable but stable 'small plasma' which extends to around half of the minor radius, or a full radiative collapse (the latter being the more common case for power starvation).

For the selection of representative discharges with stable detachment, organizational and operational constraints limit the number of experiments available for useful analysis, especially with respect to the availability of GPI data. The GPI hydrogen puff initially had to be proven to cause minimal edge perturbations, and was not established as a routine diagnostic until later in the campaign. The majority of experiments exhibiting detachment with GPI participation are heating power step-down experiments at high line-integrated density which end up in detachment incidentally. This results in a database of 45 discharges, although varying magnetic configurations with different detachment behavior and GPI field of view (FOV) reduce the statistics of what may be considered a typical detachment scenario. Ultimately, 11 successful programs with good GPI coverage of different f_{rad} levels and high signal quality are considered for this analysis, three of which are presented in detail.

The three routes to detachment are shown in summary plots with time traces of key plasma parameters in figure 1. At the top, the ECRH power (blue) is shown together with the total radiated power in red (of which most is emitted at the plasma edge) as measured by a bolometry camera system [15]. For the first discharge, the valve opening times for neon seeding are shown in green. The time points at which GPI is active are marked with black vertical black bars. In the middle panels, the line-integrated density $\int n dl$ and diamagnetic energy W_{dia} are shown, followed by the (central) electron and ion temperatures, T_e and T_i, measured by an x-ray imaging spectrometer (XICS) [16].

Discharge 20230214.055 (figure 1 left) uses neon seeding to reach detachment by puffing a larger amount every full second and smaller ones with higher frequency to maintain its concentration. The larger puffs are clearly visible as stepwise increases in P_{rad}, while the heating power and density is held constant. Full detachment is reached around 5–6 s and is maintained until the programmed end of the discharge at 8 s. The central temperatures remain entirely unaffected, while the diamagnetic energy decreases slightly with each puff by a total of around 6%.

The kinetic core plasma profiles, measured by the XICS [16] and Thomson scattering [17] diagnostic systems, are virtually unchanged throughout this discharge, as shown in figure 2 left for two time points with an attached (blue, $f_{rad} \approx 0.4$) and detached (red, $f_{rad} \approx 1$) plasma. T_e (points, fits with solid lines) is peaked due to the central ECH deposition, and $T_i \leqslant T_e$ since the ions are collisionally heated by the electrons. The electron density n_e (points, fits with solid lines) is mostly flat in the core, and falls off to around half its central value at the last closed flux surface (LCFS). While the T_e and n_e points measured by Thomson scattering have a large scatter, the individual scattering volumes show little temporal variation, and the fits are very similar. The T_i profiles (dashed), inverted from line-integrated XICS signals, also show no variation within the systematic error. In addition, profiles of the effective charge Z_{eff} inferred from Bremsstrahlung [18] (not pictured) increase moderately but measurably by about 0.1 with every impurity gas puff from 1.5 to 2.2 close to the axis, and 1.1 to 1.6 at $r_{eff}/a = 0.75$, saturating in time together with f_{rad} after 6 s. In the SOL, T_e and n_e are measured by reciprocating probes [19], shown in figure 2 right for a different discharge in the 'standard' configuration due to limited probe data availability in more comparable situations. The probe paths through the SOL geometry is shown in more detail in figure 4. In general, it is observed that there is a complex three-dimensional variation of plasma parameters in and around the magnetic islands, and their detailed structure can thus be difficult to interpret

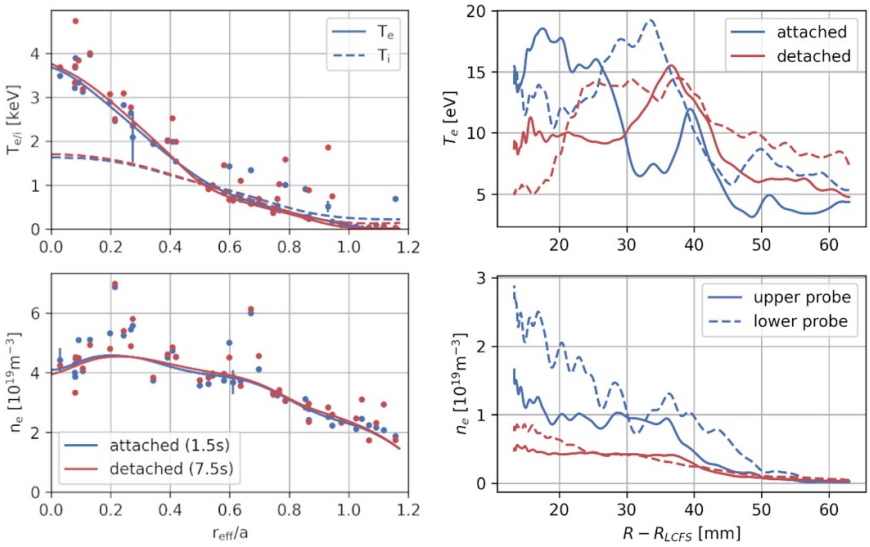

Figure 2. *Left:* Core kinetic plasma profiles for two time points in discharge 20230214.055, with T_e and n_e as measured by Thomson scattering (points), corresponding fits (solid lines) and T_i (dashed lines) as inverted from XICS data. Error bars are shown for selected representative points. *Right:* SOL profiles of T_e and n_e measured by reciprocating probes in discharge 20230323.054 at two time points and two vertical positions (solid and dashed lines) described in section 3.

from single traces. During detachment, it is however generally observed that cooling of the magnetic island (the area closest to the LCFS in the data shown) takes place during transition from an attached (blue) to a detached plasma (red) for both probe paths (solid and dashed), while the situation is less clear for the far SOL. Additionally, there is a large and consistent reduction of the SOL density throughout the entire measured area.

Discharge 20230214.046 (figure 1 center) reaches a detachment regime with $f_{rad} \approx 0.8$ by increasing the density in two feedback-controlled ramps (gas puffs) at constant heating power. f_{rad} increases more strongly than the density rises, along with a decrease in the core T_e while T_i remains nearly constant. The increase in density outpaces the loss in T_e such that W_{dia} increases slightly throughout the discharge. Starting from 7 s, a large scale edge instability appears, which is visible even in the line-integrated density trace as irregular spikes, but does not seem to affect core parameters significantly. Other discharges with more aggressive density ramps into complete detachment show this instability much more strongly, clearly visible in all core plasma parameters.

Discharge 20230117.074 (figure 1 right) reaches detachment by power starvation. At a high constant (feedback-controlled) density, f_{rad} increases towards 1 with every step down in P_{ECH} at nearly constant P_{rad}. Note that P_{rad} tends to rapidly increase by small amounts after power steps due to fast increases in edge fueling by the density feedback controller, which compensates a reduction in recycling fluxes at lower power input to the divertor (and is not visible in cases without feedback control). The power steps at 12.5 s and 15.5 s lead to detachment with $f_{rad} \approx 0.8$ and 1.0, respectively, and are accompanied by drops of W_{dia} mainly due to reduced electron heating while the core T_i remains constant. In the last power step into complete detachment ($f_{rad} \approx 1$), the low ECH power results in a decrease of T_e below the previous T_i value. Both temperatures drop together, since $T_i \leqslant T_e$ for ECH plasmas. There is therefore only a small heating power window (in this case between 1.6 and 2.0 MW) in which complete detachment with intrinsic impurities is achieved without significantly impacting core T_i and τ_e at lower heating power. This specific discharge quickly ends in a radiative collapse during a final attempted drop in heating power below 1 MW.

We note that these discharges are chosen for their data availability and quality, and span two magnetic configurations, 'standard' and 'high mirror', as indicated in the figure. While the phenomena associated with detachment presented here are qualitatively independent of configuration, geometry differences exist especially in the edge islands, affecting flux surface positions and the diagnostic systems' FOV. This is indicated in the text where relevant.

3. Diagnostic systems

3.1. Phase contrast imaging (PCI)

PCI systems in fusion experiments measure line-integrated density fluctuations (of wavelength $\lambda_P \approx 0.4-4$ cm) by small-angle scattering of an infrared laser beam (of wavelength $\lambda_L = 10.6\,\mu$m) with a scattering angle away from the beam of $\alpha \propto \lambda_L/\lambda_P$ [20]. On a phase plate located at a focal plane of the optical collection system, the scattered component is phase-shifted with respect to the unscattered component so that the signal intensity in a subsequent image plane is directly proportional to the line-integrated fluctuation amplitude $I \propto \int \tilde{n}\,\mathrm{d}l$. The W7-X PCI system [21] is shown schematically in figure 3(left) together with the flux surfaces at the toroidal position ($\Phi = 4.55$ rad) of the diagnostic. It

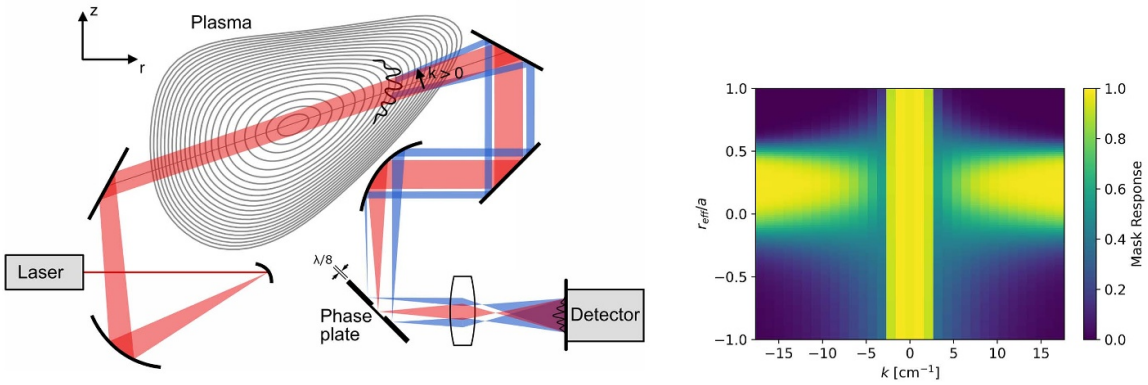

Figure 3. *Left:* Schematic of the PCI diagnostic including flux surface shapes at its toroidal location. Positive wavenumbers are defined as shown by the $k > 0$ arrow perpendicular to the line of sight. *Right:* Radial localization by the spatial selection mask of the PCI system for the angle setting and 'high mirror' magnetic configuration used in section 4.1.

fires a CO_2 laser through the core plasma onto two separate 32-channel detector arrays, allowing for (approximately) poloidally resolved measurements of $\int \tilde{n}(\theta)\,\mathrm{d}l$ and thereby k_θ across the laser beam diameter. As visible in figure 3, there is a small finite angle between the flux surfaces and the beam normal (measurement) direction, discussed in detail in [21, 22]. For the present work, we use the poloidal wave number k_θ and measurement direction k interchangeably. k is defined as positive when pointing upwards, such that on the outboard side (where $r > r_{ax}$), k is negative when $E_r < 0$ and $v \sim v_{E\times B}$. A new feature in the most recent campaign is a (freely rotatable) masking plate with a wedge-shaped cutout in a further focal plane which exploits the fact that the scattering angle around the beam depends on the local magnetic pitch angle, thus allowing the physical masking of the line-integrated signal components from certain radial ranges. Figure 3 right shows the effect of a 10° opening angle filtering mask for a given angle setting (−2°) in the 'high mirror' magnetic configuration for the detectable wavenumbers. Good localization with maximum signal throughput is achieved between $0 < r_{\mathrm{eff}}/a < 0.5$ for large k, while lower wavenumber fluctuations are detected from an increasing radial range with lower amplitude, especially on the inboard side. In the experiments reported on here, one detector has the filtering mask installed, while the other is unmasked and measures the full line-integrated signal. Further details of the radial mask selection feature are reported in [23, 24].

3.2. Gas puff imaging (GPI)

GPI is a mature diagnostic that has been used on a number of tokamaks [25] to study the dynamics of fluctuations in the edge and SOL plasma. It utilizes a small controlled puff of H_2 or He gas to supply a localized source of atoms that are subsequently excited by local plasma electrons. Line radiation from the neutrals is collected along sight lines that pass through the collimated gas cloud and are close to parallel with the field lines there. As realized on W7-X [26], the toroidal collimation of the gas cloud is crucial for achieving good spatial resolution (∼5–7 mm) in the 2D images captured by a fast-framing (2 Mfps) camera with 8×16 pixels, capturing a total FOV of 42×78 mm. The fluctuations in the H_α line emission are due to fluctuations in both the local electron density and temperature, and the images serve as proxies for visualizing their 2D dynamics. Both the nozzle and FOV position are marked in figure 4 left for the case of the 'standard' magnetic configuration, together with the flux surfaces of the core plasma and the magnetic islands, and the color-coded magnetic connection length. The GPI FOV is fixed in space, though changes in the variable magnetic configurations of W7-X, as well as changes in the equilibrium, plasma and control coil currents modify which part of the SOL is observed by GPI, as shown in figure 4 right for two configurations ('high mirror', HM and 'standard', ST) discussed below. The black box is the GPI FOV and the black line is the coordinate aligned with the detector, x_{GPI}. Additionally, the paths of the reciprocating probes attached to the multi-purpose manipulator are shown in green, as mapped to the equivalent toroidal position of GPI for the HM configuration. The rightmost plot shows the connection length L_C along this coordinate, offset by the LCFS intersection, as well as the O-point distance (dashed lines, almost equal for both configurations) and the detector column positions (dots). Due to the way segmented divertor targets in W7-X intersect the field lines, magnetic islands do not necessarily have regions of private flux with infinite L_C but may be intersected after a short toroidal distance. For the cases shown (which take into account the coil and instantaneous plasma currents), the ST configuration has such a region around the O-point which is fully covered by the GPI FOV, whereas the HM configuration does not.

In addition to the two fluctuation imaging diagnostic systems showcased in this work, additional systems based on a variety of measurement principles are installed on W7-X which will however not be considered in the scope of this work. These include multiple Doppler backscattering systems (e.g. [27]) and a poloidal correlation reflectometer ([28]) for the core and edge plasma, radial and poloidal correlation electron cyclotron emission systems, and for the edge and SOL an alkaline beam [29] as well as reciprocating probes ([30]).

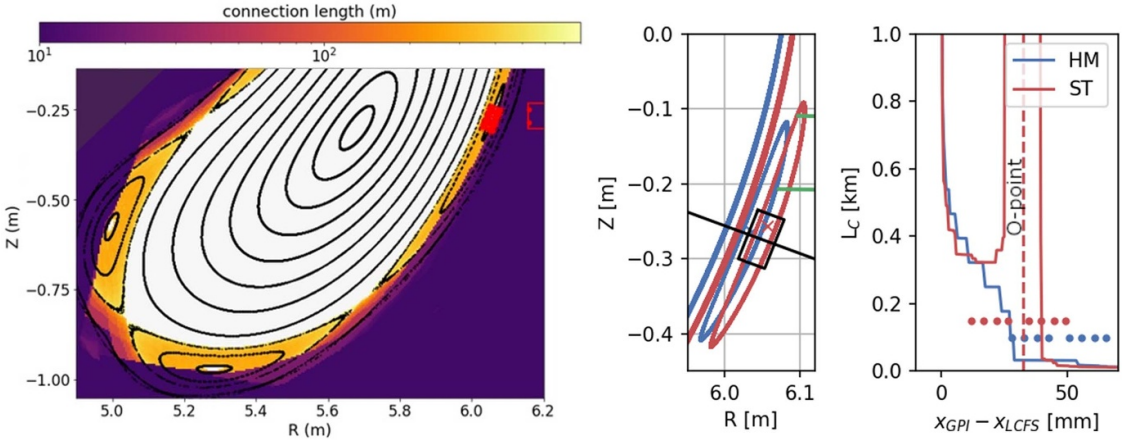

Figure 4. *Left:* Flux surfaces of the core plasma and magnetic islands at the toroidal angle of GPI over the color-coded magnetic connection length, together with the nozzle position and FOV for the 'standard' magnetic configuration. *Right*: Zoomed GPI FOV together with the last closed flux surface and island position (x) in the 'standard' (ST, red) and 'high mirror' (HM, blue) magnetic configurations with the reciprocating probe paths for the ST configuration (green). Connection length profiles along the image coordinate x_{GPI}, O-point position (dashed) and GPI detector column positions (dots).

4. Results

4.1. Impurity seeding scenario

The impurity seeding scenario in discharge 20230214.055 exhibits comparatively benign impact on both core and edge turbulence and will be discussed first. Figure 5 shows density fluctuation properties as measured by PCI, beginning with the single channel spectrograms of the most illuminated (central) channel from both detectors. The line-integrated (unmasked) measurement shows a clear impact of the neon injections on the spectrogram at higher frequencies at every full second, while at lower frequencies ($f < 200\,\mathrm{kHz}$) the spectrum remains unchanged throughout the discharge. The core (masked) measurement sees comparatively less fluctuation power in general and, more importantly, does not react to the injections, indicating that the reduction in high-frequency fluctuations occurs outside of the wavenumbers and radial positions transmitted by the radial selection mask shown in figure 3.

This is shown more quantitatively in the central panel of figure 5, which shows the total fluctuation amplitude from both detectors over the entire reliable and calibrated frequency range (20–1000 kHz) as solid lines, as well as the high-frequency part ($f > 600\,\mathrm{kHz}$) only. The line-integrated measurement is absolutely calibrated, while the calibration with a spatial mask inserted is not reliable due to unknown masking of the calibration signal itself. Although the overall ratio of line-integrated fluctuation amplitude to line-integrated background density is only 0.3%, depending on the assumed radial location (typically around $r/a \sim 0.6$–0.8) and spatial extent of the fluctuations ($\Delta r/a \sim 0.2$), the local fluctuation amplitudes have been shown to reach several percent locally (following [31]). Note that the total fluctuation amplitude is constant throughout the discharge for both detectors, indicating that the fraction responding to changes in f_{rad} is comparatively small. The high-frequency component of the line-integrated measurement scales fairly accurately with $1/f_{rad}$ over its entire range of variation, while the core measurement stays entirely constant. At these frequencies, the power spectra $S(k, f > 600\,\mathrm{kHz})$ peak at wavenumbers of $|k| > 10\,\mathrm{cm}^{-1}$ where the mask provides good radial localization (see figure 3).

In the right panel of figure 5, the dominant phase velocities from the line-integrated measurement, determined from frequency-wavenumber spectra (see figure 6), are shown as they evolve over time. The two velocities correspond to upward and downward propagation in the reference frame of the probing laser beam, and have been shown [22] to likely correspond to the same local $E_r \times B$ velocity of radially localized ($\rho \approx 0.75$), comparatively (to $v_{E\times B}$) slow, ITG-driven fluctuations on the outboard (negative k) and inboard (positive k) sides for the regular toroidal field direction of W7-X. Remarkably, the outboard branch seems to evolve substantially throughout the discharge, decreasing rapidly from its initial value of about $3.6\,\mathrm{km\,s}^{-1}$ by $1.5\,\mathrm{km\,s}^{-1}$ until about 4.5 s when f_{rad} approaches 1, while the inboard branch varies very little around $2.8\,\mathrm{km\,s}^{-1}$. This is different from the situation far from detachment [22] in which the velocities originate from fluctuations on the same flux surface and thus vary symmetrically, following changes in equilibrium profiles and thereby E_r as set by neoclassical transport. This result is therefore unintuitive for two reasons: First, the basic assumption that fluctuations drift poloidally with $v_{ph} \approx E_r \times B$ and stem from the same flux surface on the in- and outboard sides must be invalid in this case. Additionally, core plasma parameters indicate negligible changes in equilibrium profiles and Z_{eff}, which do not support such a large change of E_r [32] or the driving gradients of instabilities. Direct poloidal flow measurements using the XICS diagnostic system and resulting inversions of E_r support this statement, showing no variation at any radial position in the core plasma throughout the discharge within the statistical uncertainty of typically $500\,\mathrm{m\,s}^{-1}$ (compared to an expected magnitude of $\approx 1\,\mathrm{km\,s}^{-1}$). The fluctuation phase velocity may be substantially changing relative to $v_{E\times B}$ as the result of a shift of the dominant instability type (for example between

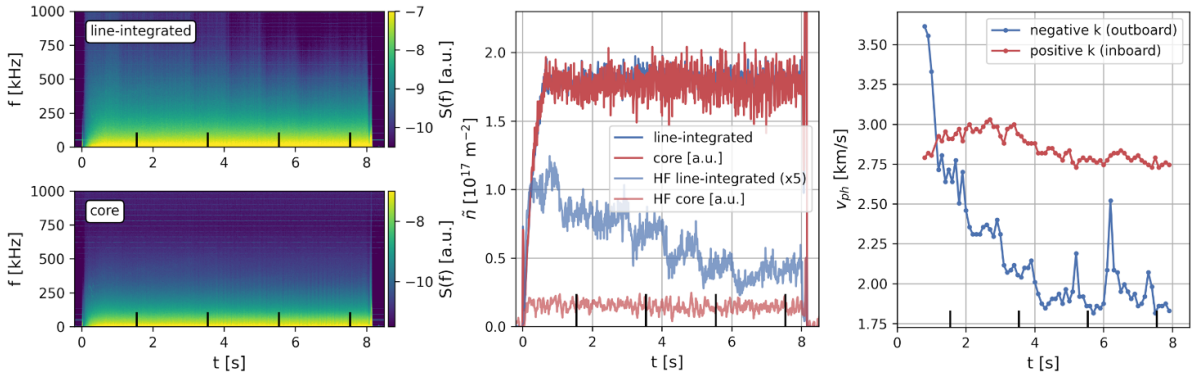

Figure 5. Density fluctuation properties as measured by PCI in discharge 20230214.055. *Left:* Frequency spectrograms from both detectors (line-integrated and masked for core fluctuations only) with time points of GPI measurements marked (black bars). *Center:* Total fluctuation amplitudes from both detectors (solid), absolutely calibrated for the line-integrated case, and (scaled-up) high-frequency components above 600 kHz (semi-transparent). *Right:* Time evolution of dominant fluctuation phase velocities with positive (inboard) and negative (outboard) wavenumbers.

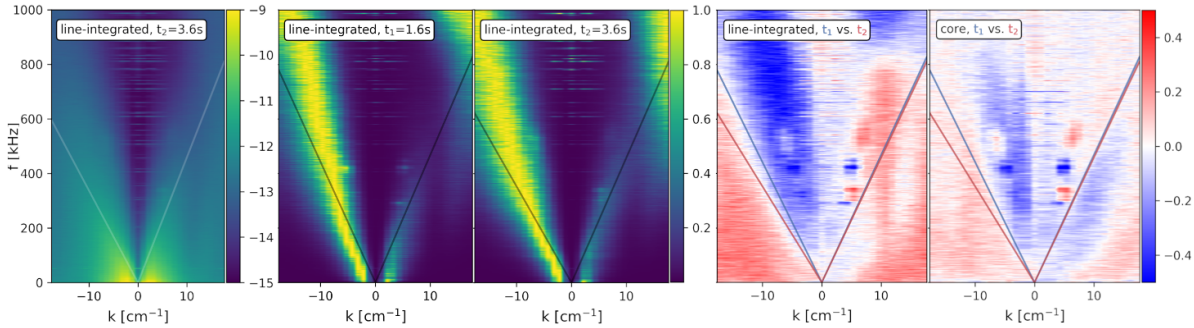

Figure 6. Frequency-wavenumber spectra $S(k,f)$ of density fluctuations measured by PCI in discharge 20230214.055 at the times of two GPI gas puffs, $t_1 = 1.6\,\mathrm{s}$ and $t_2 = 3.6\,\mathrm{s}$. From left to right: (logarithmic) amplitude spectrum $S_{int}(k,f,t_2)$; frequency-normalized ('conditional') spectra $\bar{S}_{int}(k,f,t_1)$ and $\bar{S}_{int}(k,f,t_2)$; amplitude spectrum differences $S_{int}(k,f,t_2) - S_{int}(k,f,t_1)$ and $S_{core}(k,f,t_2) - S_{core}(k,f,t_1)$ for both PCI detectors.

slower ITG modes and typically faster TEMs), but the asymmetry between in- and outboard side requires additional interpretation. A possible contributing effect, among others, is the asymmetry in the **k** components sampled by PCI throughout the strongly shaped flux surfaces: the measurement direction indicated by an arrow in figure 3 is more aligned with k_θ on the inboard side, compared to an increased sampling of k_r on the outboard side, which complicates a straightforward comparison between both locations.

With its 32 poloidally separated channels, fluctuations measured by PCI can additionally be resolved in wavenumber space. This is shown in figure 6, where the frequency-wavenumber spectrum constructed over 100 ms of data is shown for time points coinciding with two GPI puffs. Fluctuation power is spread over a large region of (k,f) space in both propagation directions (inboard and outboard), and decays with power laws along both f and k axes (the color scale is logarithmic). Additionally, weak but distinct modes are barely visible with a narrow peak at $f = 350\,\mathrm{kHz}$ and $k = \pm 5\,\mathrm{cm}^{-1}$. These modes are frequently observed [21, 33] and are presumably of Alfvénic nature due to their $1/\sqrt{n}$ frequency scaling, but usually contribute only marginally to the total fluctuation power measured. For the mask angle setting used here, the core-localized measurement (not shown) exhibits visually similar features with reduced amplitude in the k-range at which the localization mask is effective ($|k| > 4\,\mathrm{cm}^{-1}$). The dominant phase velocities are best visible in the frequency-normalized (often referred to as 'conditional') spectrum where the power at each frequency integrated over k is normalized to 1, and clearly show that the negative-k (outboard) fluctuations dominate, in this specific discharge by a factor of around 2. The automated phase velocity analysis referred to in figure 5 accurately determines the velocities (shown here as semi-transparent lines) from maxima in the angular distribution of local maxima in (k,f) space. Some aliasing can be seen in the upper right corner of the frequency-normalized spectrum, which is an extension of the negative velocity at these highest frequencies. To avoid contamination of the automated velocity analysis, only frequencies in the range $20\,\mathrm{kHz} < f < 600\,\mathrm{kHz}$ are taken into account. The difference between two spectra at different f_{rad} for the line-integrated and core-localized measurement reveals how fluctuation power evolves in frequency-wavenumber space as detachment is approached. The two right plots show this difference in (logarithmic) amplitude between two time points, overlaid with the respective v_{ph} from the line-integrated measurement for reference (blue: 1.6 s, red: 3.6 s). As f_{rad} increases, a significant amount of spectral power has been lost in a wedge across all detectable frequencies and

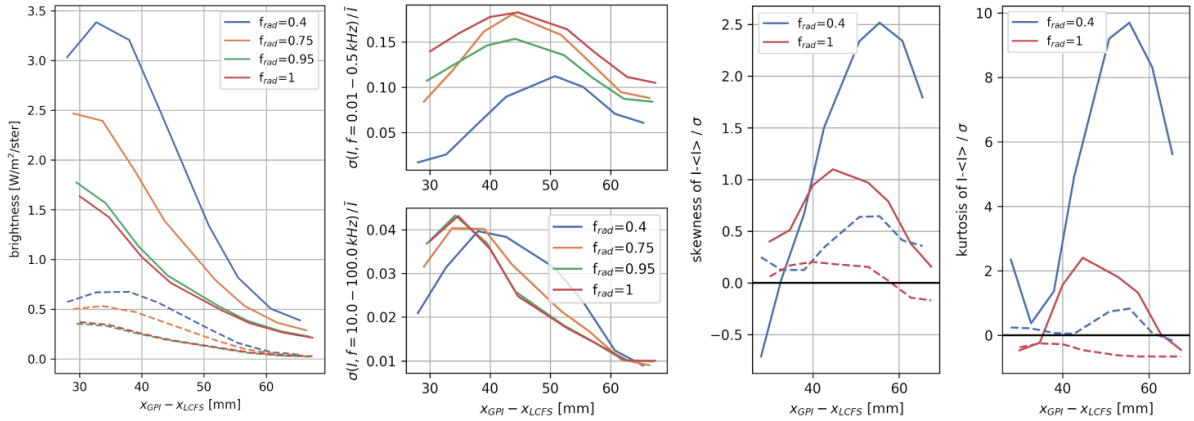

Figure 7. Radial profiles of GPI light emission during the 4 puffs in discharge 20230214.055. *Left:* Average radial emission profiles (solid) and standard deviation (i.e. fluctuations, dashed). *Center:* Mean-normalized radial fluctuation profiles in the low (10–500 Hz) and high (10–100 kHz) range. *Right:* Radial profiles of skewness and excess kurtosis, at two separate poloidal positions (solid: top, dashed: bottom of FOV).

wavenumbers in the negative-k (outboard) branch corresponding to high v_{ph}, while the positive branch (inboard) is much less affected. Additionally, a less pronounced increase in power at low, negative v_{ph} is observed at lower frequencies. The observed decrease in the frequency spectrogram in figure 5 only at high frequencies, which corresponds to an integration over k, is therefore due to changes across the entire (k,f) space that partially cancel out at lower frequencies. In the core-localized measurement (rightmost panel), using the strongly (k,f)-localized modes as a rough amplitude reference for the uncalibrated detector, we find that this effect is much less pronounced, indicating that these changes occur outside of the range selected by the mask.

In the SOL, we find with GPI that the line emission and its fluctuations systematically move radially inward with increasing f_{rad} due to an increase in the neutral penetration depth [14]. Figure 7(left) shows radial profiles of the absolute brightness moving inward and decreasing in magnitude, consistent with a drop of the SOL T_e which determines (together with the density profile) where the puffed hydrogen neutrals are excited. The dashed lines are the standard deviation of the fluctuating component of the line emission which is proportional to the local density fluctuations as well as the absolute intensity. To compare the profiles across these large intensity changes, the intensity fluctuations are normalized to their mean, which gives them a large dependence on the local density fluctuation degree $\tilde{n}/n$. These values are filtered in frequency space to separate larger-scale events from small-scale turbulence, shown in the central plots. The slow fluctuations or large-scale events (10–500 Hz) are observed to peak radially further outward in the GPI FOV, moving inward and increasing in magnitude at moderate f_{rad} and remaining at that position and magnitude for the 3 later puffs. The high-frequency component (10–100 kHz) is peaked radially further inward than the low-frequency one, and moves gradually inward with increasing f_{rad} while remaining constant in magnitude. Finally, statistical analysis of the normalized intensity probability density functions at different radial and poloidal positions reveals significant changes in the nature of the observed fluctuations between the attached and fully detached case. The distribution skewness, which reflects a bias toward more positive or negative fluctuation events, shows small negative values only on the radially innermost and vertically uppermost channels in the attached case, while otherwise showing positive values throughout with a significant poloidal spread. In the detached case ($f_{rad} = 1$), the skewness is strongly reduced and positive across the entire FOV. The excess kurtosis, which when positive roughly translates to a slower decreasing tail than a normal distribution, shows very high values, especially at the top of the FOV in the attached case. During detachment, the kurtosis is strongly reduced, and its radial maximum moves inward, following the trend in the low-frequency normalized fluctuation profiles. These results imply that transport through and around the islands into the SOL is highly three-dimensional, and substantially modified in its characteristics during detachment, though this is not reflected as strongly in the normalized fluctuation levels.

We note that in general on W7-X, spatial structures moving through the GPI FOV have a predominantly poloidal motion when inspected visually in 2D videos and processed by statistical methods (time-delay estimation and Fourier analysis), which is in strong contrast to the typical tokamak situation where radially propagating blobs are routinely observed. This is likely due to the large radius of curvature combined with strong E_r, resulting in a very low ratio of radial to poloidal motion. The ratio is so low that radial velocities are difficult to determine reliably, especially since radial correlation is poor and structures are observed to leave the FOV poloidally before they have completed any significant motion in the radial direction. In figure 8 we focus on the poloidal velocities, which depend largely on the local E_r. These are determined analogously to the PCI results shown above, with the added benefit of a 2D detector delivering radial profiles. The left plot shows the radially resolved distributions of phase velocities $\mathcal{F}(v_{ph}, x_{GPI})$ generated from individual frequency-wavenumber spectra, exhibiting a radial decrease in the distribution center throughout the far SOL from 1.6 km s^{-1} down to < 600 m s^{-1} in this particular magnetic configuration (high

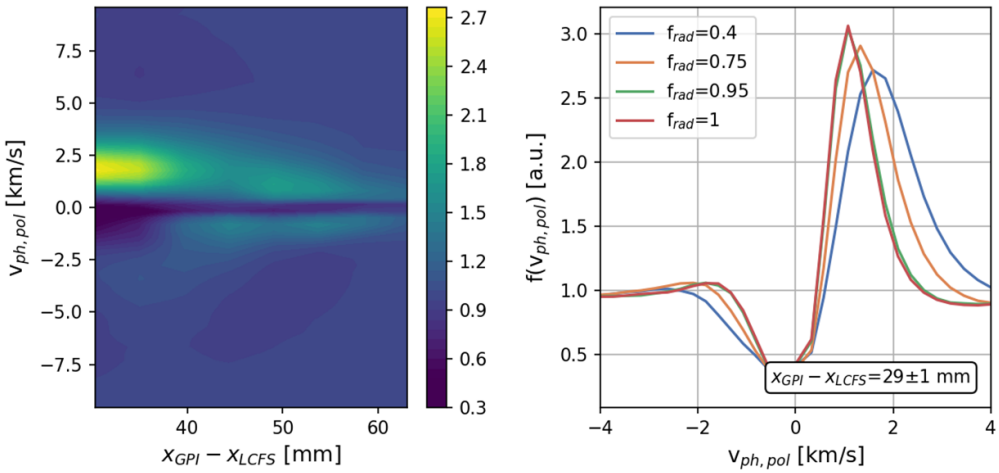

Figure 8. Radial profiles of poloidal phase velocities in discharge 20230214.055 *Left:* Probability distribution $f(v_{ph})$ for the first puff at 1.6 s. *Right:* Cuts of $f(v_{ph})$ at the innermost radial position for all four puffs.

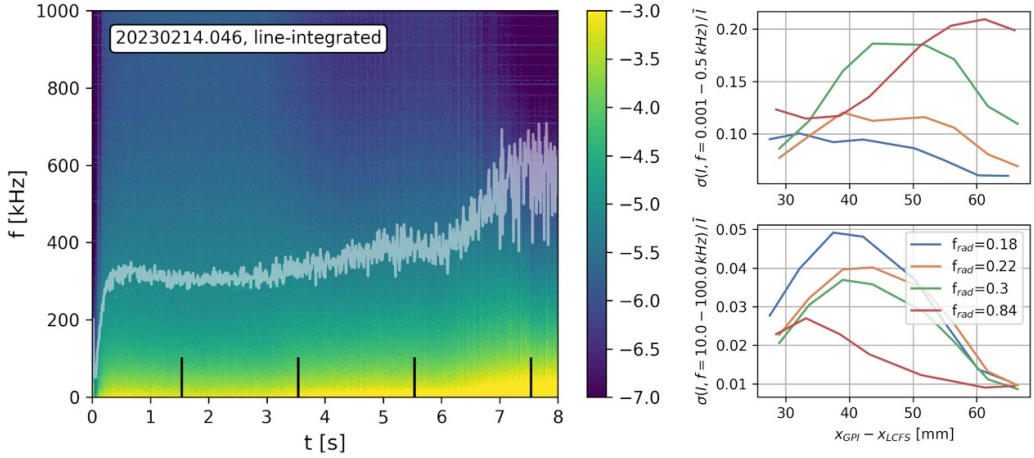

Figure 9. *Left:* PCI frequency spectrogram and total fluctuation amplitude (white line) from the density ramp experiment 20230214.046. *Right:* Mean-normalized GPI radial fluctuation profiles in the low (10–500 Hz) and high (10–100 kHz) frequency range for the same discharge.

mirror). The left plot shows the radially resolved distributions of phase velocities $\mathcal{F}(v_{ph}, x_{GPI})$ generated from individual frequency-wavenumber spectra, exhibiting a radial decrease in the distribution center throughout the far SOL from 1.6 km s^{-1} down to < 600 m s^{-1} in this particular magnetic configuration (high mirror). Note that this method cannot resolve very low phase velocities due to the vanishing spectral energy content in (k, f) space. The right plot show the time evolution of $f(v_{ph})$ at the innermost radial position as f_{rad} increases, showing a systematic slowing down of fluctuation motion, as well as a narrowing in the spread of velocities. The velocity reduction is consistent with the simple picture of a reduced T_e throughout the SOL resulting in lower corresponding potential differences along the field lines, and therefore smaller E_r.

4.2. Density ramp and power starvation scenarios

Figure 9(left panel) shows the PCI spectrograms of the density ramp discharge introduced in figure 1. The fluctuation amplitude rises with increasing density and f_{rad}, and begins to show very large irregular dropouts of up to 40% starting around 7 s. They are visible even in the line-integrated density measured by the interferometer (see figure 1) and are clearly visible as bright edge phenomena on video cameras. During these events, the fluctuation power drops across the entire frequency spectrum over time periods of less than 10 ms, possibly due to large density structures passing through the PCI laser beam path. This trend is reflected in GPI data (right panel of figure 9), which shows a large increase in the low-frequency fluctuations of the far SOL with increasing density. In contrast, the high-frequency fluctuation profile follows the radiation front radially inward and is reduced in magnitude.

In the power starvation discharge shown in figure 10, the PCI spectrum shows a clear decrease with each power step-down, and additionally enters a phase with bursty fluctuations from 12.5 s onward, as seen in the integrated fluctuation amplitude. In contrast to the density ramp scenario, these bursts are quasi-periodic with a frequency of 90–120 Hz and appear to occur only in a limited ECH power window that coincides with the power level required to reach detachment, making a

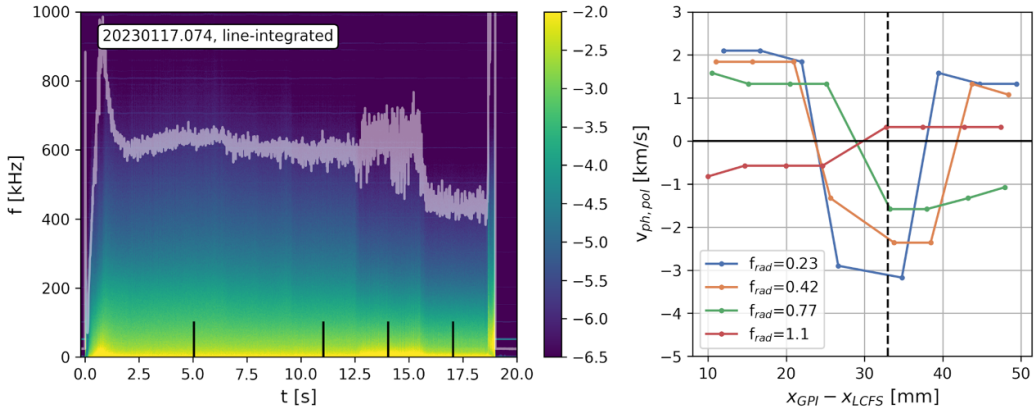

Figure 10. *Left:* PCI frequency spectrogram and total fluctuation amplitude (white line) from the power step-down experiment 20230117.074. *Right:* Radial profiles of poloidal velocity from GPI data in the SOL during the same discharge, with the island O-point marked by a dashed line.

more detailed spectral analysis with both diagnostics difficult. This regime will be characterized in more detail elsewhere. The fluctuation amplitude drops by a disproportionately large amount in the last power step into detachment at 15.5 s, though this is likely due to a decrease in the core T_i gradient at this low power rather than detachment itself. This discharge in the standard magnetic configuration gives GPI a view of the island O-point (dashed line in figure 10, right panel) with a region of infinite L_C. Here, the dominant phase velocity as found from distributions like those shown in figure 8 is plotted at each radial position for every puff. Multiple shear layers with sign changes are routinely observed in the resulting radial v_{ph} profiles at low f_{rad} in this private flux region, as will be reported elsewhere. As f_{rad} is increased, the magnitude of the velocities at all radii is reduced, and in this particular discharge exhibits a directional reversal across the entire observed area as complete detachment is achieved during the last puff. This reversal is not consistently observed in all power starvation discharges, and is speculated to stem from a transition from a low-collisionality regime (at higher T_e) in which local $E \times B$ drifts play a larger role to a sheath potential dominated regime at higher collisionality (and lower T_e) [34].

In both discharges, the dominant phase velocities measured by PCI decrease with increasing f_{rad}, though in contrast to the impurity seeded case, the outboard and inboard velocities decrease at the same rate, as previously observed [22]. This is expected for fluctuations propagating with $v_{ph} \approx v_{E\times B}$, with changes in the neoclassical radial electric field resulting from modified core profiles.

5. Conclusions

GPI and PCI provide a direct assessment of density turbulence in both core and edge. Together, both imaging diagnostic systems provide a unique and comprehensive overview of overall fluctuation levels, spectral properties such as distribution in frequency and wavenumber space as well as spatial information. A variety of effects play into detachment, and it is difficult to generalize to a common scenario when the strategies to achieve it are disparate. However, a couple of general trends in terms of density turbulence hold when f_{rad} is increased towards detachment: in the plasma edge where the actual detachment takes place, the GPI system observes clear changes in fluctuation characteristics. The observed line emission shifts radially inward, reflecting an expected reduction of the SOL T_e profile, and the normalized SOL density fluctuations generally follow this inward shift. Skewness and kurtosis of the fluctuations are reduced, indicating a reduction of large intermittent transport events, and the poloidal phase velocities are reduced throughout the SOL. These observations are consistent with a reduced power input $P_{ECH} - P_{rad,core}$ into the SOL and a general reduction of turbulent activity.

PCI measurements show that density fluctuation levels remain nearly constant with f_{rad} in the impurity seeding scenario, indicating that detachment itself does not significantly impact core turbulence. The new radial masking feature reveals that core fluctuations are barely affected, while there are minor changes at high frequencies outside of this region which seem to be spatially localized on the outboard side of the system's line of sight and have a peculiar distribution in (k,f) space. We further find a strong reduction in the dominant outboard phase velocity that is incompatible with the standard interpretation of neoclassical E_r changes.

In the density ramp and power starvation scenarios, detachment is reached by either increasing the density into a regime where the edge shows large-scale instabilities, or by decreasing the heating power to the point that the core T_i drops significantly. In both cases, the fluctuation spectra become highly intermittent and difficult to interpret.

In terms of overall turbulence and performance, impurity seeding so far appears to be a promising strategy in reaching detachment, especially when targeting a specific operating point in core density and heating power. Changes to core fluctuations are benign though some effects remain unexplained at this point, and SOL fluctuations shift spatially inward but

otherwise remain unaffected in amplitude, and show a statistical decrease in large-amplitude events.

Having established both diagnostics systems as reliable and useful tools to image and characterize turbulent fluctuations, future directions in the upcoming experimental campaign include more fine-grained f_{rad} scans, and coordinated measurements (including overlap with other systems such as Doppler backscattering and correlation ECE) during impurity-seeded detachment under variation of magnetic configuration and island topology, seeding gases, and heating scenarios.

Acknowledgments

Support for the MIT and SUNY-Cortland participation was provided by the US Department of Energy, Fusion Energy Sciences, Awards DE-SC0014229 (PCI) and DE-SC0014251 (GPI). This work has been carried out within the framework of the EUROfusion Consortium, funded by the European Union via the Euratom Research and Training Programme (Grant Agreement No. 101052200 – EUROfusion). Views and opinions expressed are however those of the authors only and do not necessarily reflect those of the European Union or the European Commission. Neither the European Union nor the European Commission can be held responsible for them.

ORCID iDs

A. von Stechow 0000-0003-0277-4600
S.G. Baek 0000-0001-8029-3525
J.-P. Bähner 0000-0002-5828-2747
S. Ballinger 0000-0003-3593-6418
D. Cipciar 0000-0002-3798-9524
E.M. Edlund 0000-0001-5320-4996
G. Fuchert 0000-0002-6640-2139
O. Grulke 0000-0001-7879-8671
T. Gonda 0009-0002-8601-6531
S.K. Hansen 0000-0002-5146-1056
C. Killer 0000-0001-7747-3066
S. Kwak 0000-0001-7874-7575
M. Krychowiak 0009-0001-4141-5558
A. Langenberg 0000-0002-2107-5488
N. Pablant 0000-0001-6617-8459
A. Pavone 0000-0003-2398-966X
M. Porkolab 0000-0002-9518-4097
J.L. Terry 0000-0003-4255-5509
D. Zhang 0000-0002-5800-4907

References

[1] Pedersen T.S. *et al* 2022 Experimental confirmation of efficient island divertor operation and successful neoclassical transport optimization in Wendelstein 7-X *Nucl. Fusion* **62** 042022
[2] Beidler C.D. *et al* (the W7-X Team) 2021 Demonstration of reduced neoclassical energy transport in Wendelstein 7-X *Nature* **596** 221–6
[3] Beurskens M.N.A. *et al* (the W7-X Team) 2021 Ion temperature clamping in Wendelstein 7-X electron cyclotron heated plasmas *Nucl. Fusion* **61** 116072
[4] Bozhenkov S.A. *et al* (the W7-X Team) 2020 High-performance plasmas after pellet injections in Wendelstein 7-X *Nucl. Fusion* **60** 066011
[5] Alcusón J.A., Xanthopoulos P., Plunk G.G., Helander P., Wilms F., Turkin Y., v. Stechow A. and Grulke O. 2020 Suppression of electrostatic micro-instabilities in maximum-J stellarators *Plasma Phys. Control. Fusion* **62** 035005
[6] Thienpondt H. *et al* (The Wendelstein 7-X Team) 2023 Prevention of core particle depletion in stellarators by turbulence *Phys. Rev. Res.* **5** L022053
[7] Xanthopoulos P. *et al* (the W7-X Team) 2020 Turbulence mechanisms of enhanced performance stellarator plasmas *Phys. Rev. Lett.* **125** 075001
[8] Zocco A., Podavini L., Wilms F., Bañón Navarro A. and Jenko F. 2024 Electron-temperature-gradient-driven ion-scale turbulence in high-performance scenarios in Wendelstein 7-X *Phys. Rev. Res.* **6** 033099
[9] Wilms F., Bañón Navarro A., Windisch T., Bozhenkov S., Warmer F., Fuchert G., Ford O., Zhang D., Stange T. and Jenko F. (the W7-X Team) 2024 Global gyrokinetic analysis of Wendelstein 7-X discharge: unveiling the importance of trapped-electron-mode and electron-temperature-gradient turbulence *Nucl. Fusion* **64** 096040
[10] Grulke O. *et al* 2024 Overview of the first Wendelstein 7-X long pulse campaign with fully water-cooled plasma facing components *Nucl. Fusion* **64** 112002
[11] Ford O.P. *et al* (the W7-X Team) 2024 Turbulence-reduced high-performance scenarios in Wendelstein 7-X *Nucl. Fusion* **64** 086067
[12] Jakubowski M. *et al* (the W7-X Team) 2021 Overview of the results from divertor experiments with attached and detached plasmas at Wendelstein 7-X and their implications for steady-state operation *Nucl. Fusion* **61** 106003
[13] Zhang D. *et al* (W7-X Team) 2019 First observation of a stable highly dissipative divertor plasma regime on the Wendelstein 7-X Stellarator *Phys. Rev. Lett.* **123** 025002
[14] Feng Y. *et al* (W7-X Team) 2021 Understanding detachment of the W7-X island divertor *Nucl. Fusion* **61** 086012
[15] Zhang D. *et al* 2010 Design criteria of the bolometer diagnostic for steady-state operation of the W7-X stellarator *Rev. Sci. Instrum.* **81** 10E134
[16] Langenberg A. *et al* (W7-X Team) 2018 Prospects of x-ray imaging spectrometers for impurity transport: recent results from the stellarator Wendelstein 7-X (invited) *Rev. Sci. Instrum.* **89** 10G101
[17] Bozhenkov S.A. *et al* 2017 The Thomson scattering diagnostic at Wendelstein 7-X and its performance in the first operation phase *J. Instrum.* **12** 10004
[18] Kwak S. *et al* (Wendelstein 7-X Team) 2021 Bayesian inference of spatially resolved Zeff profiles from line integrated bremsstrahlung spectra *Rev. Sci. Instrum.* **92** 043505
[19] Killer C., Drews P., Grulke O., Knieps A., Nicolai D. and Satheeswaran G. (W7-X Team) 2022 Reciprocating probe measurements in the test divertor operation phase of Wendelstein 7-X *J. Instrum.* **17** 03018
[20] Porkolab M., Rost J., Basse N., Dorris J., Edlund E., Lin L., Lin Y. and Wukitch S. 2006 Phase contrast imaging of waves and instabilities in high temperature magnetized fusion plasmas *IEEE Trans. Plasma Sci.* **34** 229–34
[21] Huang Z., Edlund E., Porkolab M., Bähner J.-P., Böttger L.-G., v. Sehren C., v. Stechow A. and Grulke O. 2021 The

Wendelstein 7-X phase contrast imaging diagnostic *J. Inst.* **16** 01014
[22] Bähner J.-P. *et al* (The W7-X Team) 2021 Phase contrast imaging measurements and numerical simulations of turbulent density fluctuations in gas-fuelled ECRH discharges in Wendelstein 7-X *J. Plasma Phys.* **87** 905870314
[23] Hansen S.K., Porkolab M., Bähner J.-P., v. Stechow A., Grulke O. and Edlund E.M. (the Wendelstein 7-X Team) 2024 Localized phase contrast imaging at the Wendelstein 7-X stellarator *Phys. Plasmas* **31** 062302
[24] Hansen S K, Porkolab M, Rost J C, Bähner J, Major M R, von Stechow A, Grulke O and Edlund E M and 2025 Improved description of diffraction effects for phase contrast imaging with applications to magnetically confined fusion plasmas *Rev. Sci. Instrum.* **96**
[25] Zweben S.J., Terry J.L., Stotler D.P. and Maqueda R.J. 2017 Invited review article: gas puff imaging diagnostics of edge plasma turbulence in magnetic fusion devices *Rev. Sci. Instrum.* **88** 041101
[26] Terry J.L. *et al* (W7-X Team) 2024 Realization of a gas puff imaging system on the Wendelstein 7-X stellarator *Rev. Sci. Instrum.* **95** 093517
[27] Estrada T. *et al* (W7-X Team) 2021 Radial electric field and density fluctuations measured by Doppler reflectometry during the post-pellet enhanced confinement phase in W7-X *Nucl. Fusion* **61** 046008
[28] Windisch T., Krämer-Flecken A., Velasco J.L., Könies A., Nührenberg C., Grulke O. and Klinger T. (the W7-X Team) 2017 Poloidal correlation reflectometry at W7-X: radial electric field and coherent fluctuations *Plasma Phys. Control. Fusion* **59** 105002
[29] Nagy D. *et al* (W7-X Team) 2023 Development of the W7-X alkali metal beam diagnostic observation system for OP2 *J. Nucl. Eng.* **4** 142–51
[30] Killer C., Grulke O., Drews P., Gao Y., Jakubowski M., Knieps A., Nicolai D., Niemann H., Sitjes A.P. and Satheeswaran G. (W7-X Team) 2019 Characterization of the W7-X scrape-off layer using reciprocating probes *Nucl. Fusion* **59** 086013
[31] Weisen H., Hollenstein C. and Behn R. 1988 Turbulent density fluctuations in the TCA Tokamak *Plasma Phys. Control. Fusion* **30** 293
[32] Pablant N. *et al* (W7-X Team) 2020 Investigation of the neoclassical ambipolar electric field in ion-root plasmas on W7-X *Nucl. Fusion* **60** 036021
[33] Edlund E.M., Porkolab M., Huang Z., Grulke O., Böttger L.-G., von Sehren C. and von Stechow A. 2018 Overview of the Wendelstein 7-X phase contrast imaging diagnostic *Rev. Sci. Instrum.* **89** 10E105
[34] Flom E., Kriete D.M., Krychowiak M., Maaziz N., Perseo V., Reimold F., Schmitz O., Winters V., Henke F., Gradic D. and König R. (the W7-X Team) 2023 Observation of a drift-driven local transport regime in the island divertor of Wendelstein 7-X (arXiv:2312.01240 [physics])